AIAA JOURNAL
Vol. 30, No. 9, September 1992

Physical Model of the Swept Shock Wave/Boundary-Layer Interaction Flowfield

F. S. Alvi* and G. S. Settles†
Pennsylvania State University, University Park, Pennsylvania 16802

New data are presented on the structure of fin-induced, swept shock/boundary-layer interactions. These data are obtained using a nonintrusive planar laser scattering (PLS) imaging technique. A range of interaction strengths, from barely separated to very strongly separated, is covered for freestream Mach numbers of 3 and 4. These new data, when combined with previous results on the flowfield and interaction "footprint," are sufficient to allow the construction of a physical model for the swept interaction flowfield structure and behavior. This physical model is presented and discussed in terms of six detailed flowfield maps which take advantage of the inherent quasiconical behavior of the class of interactions considered.

Introduction

THE interaction of a swept shock wave with a turbulent boundary layer is a classic viscous/inviscid interaction problem with both practical and fundamental importance. Recent practical applications involving such interactions include the propulsion and control systems of both the National Aerospace Plane (NASP) and the High-Speed Civil Transport (HSCT). Consequently, such swept interactions have been the focus of numerous research efforts—both in experimental and computational fluid dynamics (CFD).[1,2] However, due to their inherent complexity, these interactions are still only partially predicted by computational modeling at the present time. Experimental studies are still necessary to better understand the flow physics and to produce benchmark data for turbulence modeling and CFD code validation.

Most previous studies of swept interactions focused primarily on the behavior of the surface flow properties (the interaction "footprint"). Although measurements of surface pressure, skin friction,[3] and surface behavior[4] have all led to a greater understanding of these interactions, the structure of the interaction flowfield has been comparatively poorly understood.

Oskam[5] was among the first investigators to study the flowfield structure of sharp-fin-generated swept interactions. Unfortunately, he examined only a weak case and his yaw-probe surveys lacked the resolution necessary to provide a complete picture of the interactions structure. A much more detailed investigation of the flowfield structure was conducted by Zubin and Ostapenko[6] using a conical shadowgraphy technique. Their experiments broke new ground in defining the interaction flowfield structure, but have only been available in a very abbreviated form in the West. More recent experiments by Lu and Settles,[7] who used a planar laser scattering (PLS) technique, further added to the understanding of this complex phenomenon. Unfortunately, their experiments suffered from low resolution and geometrical constraints which rendered their results semiquantitative at best. Alvi and Settles[8] next achieved a significant improvement in the visualization of the interaction structure with very-high-resolution conical shadowgraphy. They presented a qualitative interaction flowfield model which contained all of the features of the flow discovered thus far, plus several newly observed features. It still remains to define the flowfield structure quantitatively and to integrate past and present results into a coherent physical model describing both the structure and behavior of the fin interaction flowfield.

It is thus the goal of this study to further expand the knowledge of fin-generated swept interactions by providing such a quantitative physical flowfield model with an accurate reference frame, suitable for direct comparison with CFD predictions. This model will also enable us to study the relationship between surface and flowfield features and hence provide insight into the interaction behavior as a whole.

To accomplish this goal, new flowfield PLS images have been obtained using apparatus much improved since the work reported in Ref. 7. Six individual flowfields spanning the range from weak to very strong interaction strengths were investigated. A gridding technique incorporated into the PLS images enabled us to spatially locate the various interaction features and to construct flowfield maps of the overall structure. The small-scale, detailed features of the flowfield were then added from our earlier conical shadowgraphy experiments.[8] In this way, we are able to present a comprehensive physical flowfield model in the conical reference frame which is inherent to this class of swept interactions.[1,2]

Quasiconical Flow Symmetry

Before proceeding, it is appropriate to briefly review the issue of sharp-fin interaction symmetry (see Fig. 1). These interactions have been shown experimentally,[1,9] analytically,[10] and computationally[11,12] to possess quasiconical symmetry

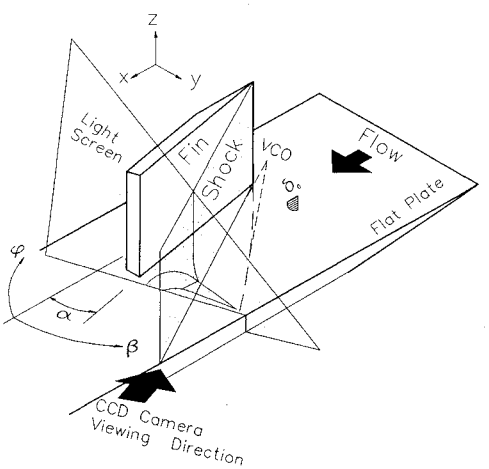

Fig. 1 Sketch of the test geometry with light screen.

Received Aug. 12, 1991; revision received Feb. 10, 1992; accepted for publication Feb. 11, 1992.

*Graduate Research Assistant, Mechanical Engineering Dept. Student Member AIAA.

†Professor of Mechanical Engineering and Director, Gas Dynamics Laboratory, 303 Mechanical Engineering Building. Fellow AIAA.

about a virtual origin slightly upstream of the fin leading edge. This virtual conical origin (VCO) is indicated in Fig. 1. It is the point where the various topological features of the interaction, e.g., the upstream influence line, separation line, and attachment line, converge. Outside an initial development region known as the "inception zone"[9] near the fin leading edge, the far-field behavior of the interaction features is observed to be conical with respect to the VCO.

This quasiconical symmetry suggests that the natural coordinate frame for such flows should be a spherical polar coordinate frame (r, β, ϕ) centered about the VCO (see Fig. 1). From the definition of conical flow, it follows that the r coordinate is degenerate since conical flow properties are constant along radial lines. Consequently, the flowfield of such an interaction is entirely represented by the angular coordinates β and ϕ and is thus properly considered to be a two-dimensional flow.

Experimental Techniques

Wind-Tunnel Facility and Test Conditions

The experiments were performed in the supersonic wind-tunnel facility of the Pennsylvania State University gas dynamics laboratory. The wind tunnel is an intermittent blow-down type with a test section size of $15 \times 17 \times 60$ cm, with a variable Mach number capability over the range of Mach 1.5–4.0. A 200 m^3, 20-atm pressure reservoir provides testing times up to 2 min at stagnation pressures up to 15 atm.

The test geometry, shown in Fig. 1, consists of a sharp unswept fin mounted on a flat plate spanning the test section. The fin is high enough to produce a dimensionless, semi-infinite swept interaction over the entire span of the test section and is positioned 10 cm downstream of the plate leading edge. The fin distance from the tunnel sidewall varied from 1.8 to 5.2 cm, depending on its angle of attack α. A pneumatic fin-injection mechanism was employed to vary the fin angle of attack. The flat plate produced an equilibrium, adiabatic-wall, zero pressure gradient, turbulent boundary-layer of about 3 mm local thickness which has been well documented in previous publications.[4] The test conditions for the present experiment were $\alpha = 10$, 16, and 20 deg at Mach 2.95 and $\alpha = 16$, 20, and 25 deg at Mach 3.95. The test Reynolds numbers varied from 58×10^6 to 72×10^6 m^{-1}, depending on interaction strength.

One sidewall of the wind-tunnel test section was replaced by a 3.8-cm-thick acrylic plastic window spanning its entire length. This provided extensive optical access, a critical requirement for this experiment.

PLS Imaging Technique

Optical Setup

A planar laser scattering (PLS) technique, also known as the laser light-sheet or vapor-screen technique, was used. Such light-screen flow-visualization techniques have been in use for almost three decades.[13] They provide powerful but relatively simple tools to investigate flowfields nonintrusively.

Figure 2 shows the optics used to generate a thin planar light sheet. A 10-W pulsed copper-vapor laser (MVL-2000, CJ Laser Corp.) is used as a light source. The laser beam is first focused in the center of the wind-tunnel test section using the two spherical lenses S1 and S2. The output of S2 is then expanded into a sheet using a combination of two cylindrical lenses C1 and C2. The two spherical lenses allow the focus of the laser beam to be changed by varying the spacing t between them. Similarly the sheet height h can be controlled by adjusting the spacing L between C1 and C2. In the resulting optical setup, the light-sheet thickness is less than 2 mm throughout the region of interest.

Any flow imaging technique used to examine fin interactions must take the quasiconical symmetry of the flow into account. Consequently, several cuts, normal to the undisturbed inviscid shock, were made at various distances from the VCO (see Fig. 1). The PLS images were recorded on S-VHS

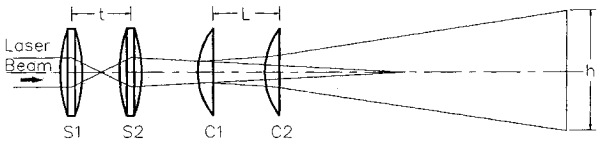

Fig. 2 Schematic of laser sheet generator.

videotape (standard 30-Hz framing rate and approximately a 1/30-s exposure) using a high-resolution color CCD camera.

The angular coordinates of flow features observed in the PLS imagery were obtained by way of "tare" images of a precise grid placed in the plane of the laser screen. By overlaying the flowfield and tare images, an accurate scaling of the former was accomplished.

Seeding Mechanism

Under normal operating conditions the compressed air supply which powers the winds tunnel is dried to a dewpoint of -35°F or lower by passing it through a silica-gel dryer. In this case the residual water content of the dried air is only a few parts/million. However, if the dryer is partially bypassed and the dewpoint is raised, some water vapor remains in the air and condenses to form miniature ice crystals upon passing through the wind-tunnel nozzle. The amount of moisture in the air can be controlled by varying the fraction of air that passes through the dryer. For the present purposes, the dewpoint of the air was monitored carefully and was held below -8°F (see Ref. 4) to avoid condensation shock waves in the nozzle.

The resulting ice crystals in the flowfield reveal its structure by scattering the laser light from the light screen described earlier. The brightness of a flow feature in such a PLS image is thus, in principle, proportional to the air density. This causes high-density zones, such as those following shock waves, to appear very bright, while darker zones similarly indicate lower density levels. An exception to this rule can occur when the static temperature of the flow becomes high enough to melt the ice crystals, whereupon particle scattering is extinguished and the flow appears black. For example, boundary-layer fluid, being generally the warmest fluid in the flow on account of its proximity to the adiabatic wall, always appears black in PLS images.

When aerosols such as the present ice crystals are used to seed the flow, care must be taken to ensure that 1) the seeding is uniform so as not to bias the image brightness, and 2) the seed particles are small enough not to disturb the flow. We confirmed that the flow was well mixed in the wind-tunnel stilling chamber by capturing uniform PLS images of the supersonic freestream without a model in place.

Two independent techniques were used to measure the size of ice crystals entrained in our flowfield. The first method, known as a two-wavelength transmissometer technique, has been used extensively in the past[14–16] to determine the size of seeding particles in high-speed flows. It involves the transmittance measurement of laser light through the seeded flow at two different wavelengths. The ratio of the transmittances at the two wavelengths is then used to calculate the mean particle size. References 14–16 discuss the application of the technique in detail. In the second particle-sizing technique, the seeded flow is illuminated by unpolarized light and the degree of polarization of light scattered at 90 deg is measured. The degree of polarization of this scattered light is inversely proportional to particle size and thus gives an estimate of the size of the ice crystals.[17–19]

The results of both these measurements indicate that the ice crystals used for seeding the flow were less than 0.3 μm in diameter. Numerical simulations performed using modified Stokes drag show that particles of this size follow the mean flow satisfactorily in that they accurately reveal the shock structure in the present flowfield.

Results and Discussion

Test Matrix

As a result of the quasiconical symmetry described earlier, the strength of the interactions under study has been found[1,2,7-9] to be independent, at least as a first approximation, of the freestream Mach number M_∞. Instead it is $M_n = M_\infty \cos \beta_0$ (β_0 is the inviscid shock angle), the Mach number component normal to the inviscid shock wave, which determines the interaction strength. Using this criterion the test matrix of the present study is shown in Fig. 3, where the pressure ratio across an oblique shock indicates the relative strengths of the six separate interactions studied; they span the range from weak (barely separated) to very strong. Four flow-regime boundaries are also indicated in Fig. 3, to be discussed later.

PLS Images

Typical PLS images for five of the six test cases, having been enhanced by image processing, are shown in Figs. 4–8. The flow direction is from right to left.

As noted previously,[1,2,4,6-8] the salient visual feature of the interaction structure is the characteristic λ-shock bifurcation of the inviscid shock wave and consists of a (forward) separation shock and a rear shock. The point of shock bifurcation, known as the triple point, is also clearly seen in Figs. 4–8. The incoming boundary layer and the separation bubble beneath the λ-foot both appear as dark regions for reasons discussed earlier with regard to the mechanism of seeding the flow.

The other obvious visual feature of these images is the impinging jet structure,[1,2,7,8,11,20] which is formed by the streamtube processed through the λ-shock. This feature is barely visible in the weak interaction of Fig. 4, but in Figs. 5–8 the jet is clearly seen to turn towards, and finally impinge upon, the flat-plate surface which supports the interaction. This jet impingement occurs in a region bounded by the separation bubble to the right and the fin surface to the left, while the outer boundary of the jet is defined by the slip-line emanating from the λ-shock triple point.

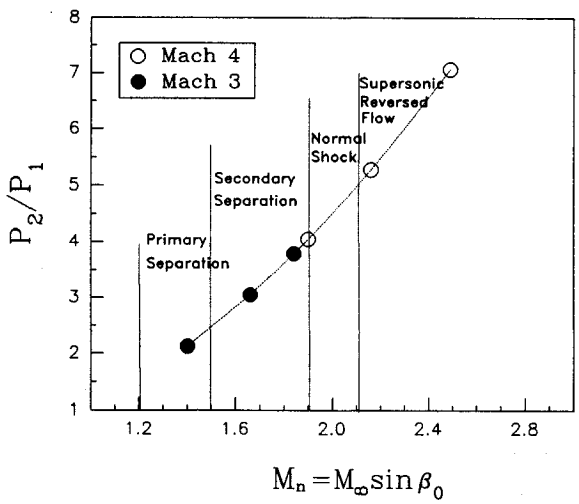

Fig. 3 Test spectrum.

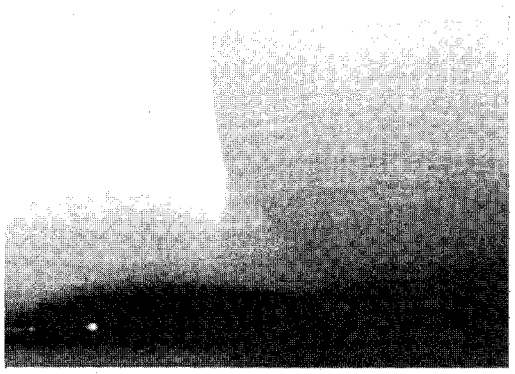

Fig. 4 PLS image (Mach 3, $\alpha = 10$ deg).

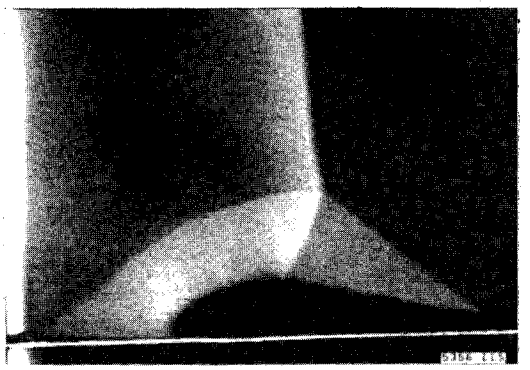

Fig. 5 PLS image (Mach 3, $\alpha = 16$ deg).

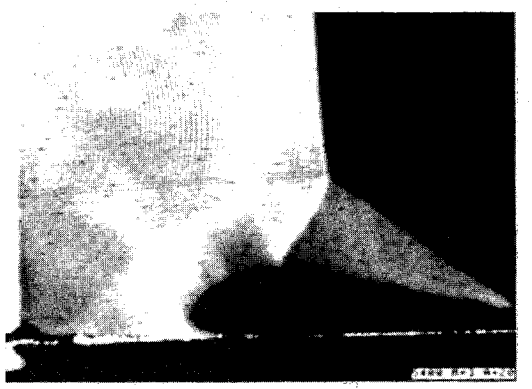

Fig. 6 PLS image (Mach 3, $\alpha = 20$ deg).

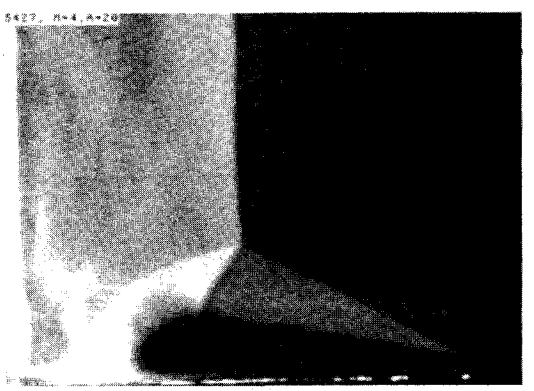

Fig. 7 PLS image (Mach 4, $\alpha = 20$ deg).

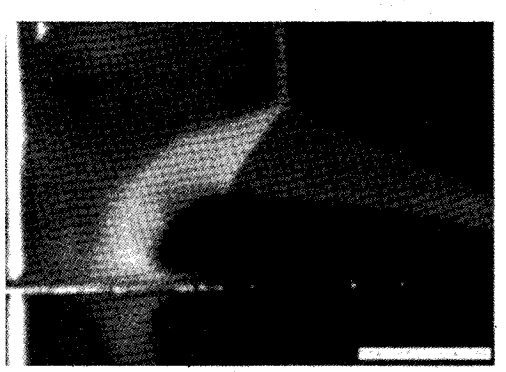

Fig. 8 PLS image (Mach 4, $\alpha = 25$ deg).

Upon examining Figs. 4–8, it becomes apparent that these structural features develop very rapidly at first, but then more slowly as the interaction becomes strong. Figure 4 depicts an interaction which is only 2 deg of fin angle beyond incipient separation according to Korkegi's criterion (see Refs. 1 and 2). The early development of a small, flat separation bubble[5] at

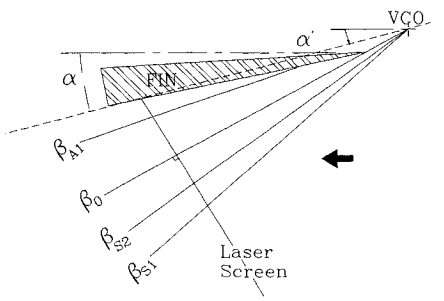

Fig. 9 Top view of test geometry.

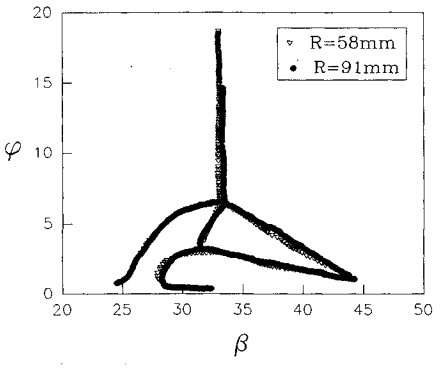

Fig. 10 Overlay of two PLS cuts at different locations.

Mach 3, $\alpha = 10$ deg supports a λ-shock which is barely visible in Fig. 4. However, in the next stronger interaction of the series, Fig. 5, all of the principal flow features mentioned above are fully formed and clearly visible. Further strength increases, Figs. 6–8, add some secondary flow features and increase the interaction size, but no further drastic structural changes are seen. The interaction growth consists mainly of the elongation of the separation bubble and separation shock, and the compaction of the impinging jet into the increasingly small region bounded by the fin and the separation bubble.

Departures from Conicity

The reader is reminded that these images are essentially normal to the rays of a quasiconical flow, and that the discussion of them, and of the flowfield model derived from them, is in the spirit of a conical-flow analysis in the normal plane.[1] Departures from conicity do occur (such as the inception zone described earlier), but are not believed to detract significantly from the strongly conical nature of the interactions observed here. Nonetheless, before proceeding to develop a physical model of the flowfield, a brief explanation of some departures from conicity and resulting geometric constraints is required.

Figure 9 shows a top view of the test geometry. Various surface features, such as the primary separation line β_{S1}, the inviscid shock projection β_0, and the flow attachment line β_{A1} are indicated. Since the VCO is the origin for the polar coordinate system of these quasiconical flows (Fig. 1), all interaction features are measured from this point. However, the intersection of the fin and flat plate defines a line which can never pass through the VCO, and hence cannot support conical flow in its local vicinity. Consequently, in the PLS images the *apparent* fin angle of attack in spherical polar coordinates is dependent upon the point where the laser sheet meets the fin surface, and subtends an angle α' with respect to the VCO. In contrast, the actual fin angle of attack α is, by definition, measured from the fin leading edge itself and does not vary with laser-sheet position.

Although this results in a discrepancy between α' and α, it is apparent from Fig. 9 that this discrepancy will be negligible when the VCO is in very close proximity to the fin leading edge (i.e., for very strong interactions). It can be further minimized by positioning the laser sheet far downstream of the fin leading edge, thus causing α' to converge toward the true α. Some α/α' discrepancy will always be present, however, in all true quasiconical interactions of the type studied here. For this reason the apparent fin angles in the flowfield maps, derived from Figs. 4–8 and presented below, never agree exactly with the actual α values characterizing those interactions.

Finally, we repeat that the departures from conicity described here are ancillary to an otherwise strongly conical flowfield structure.[1,2,9] In support of this assertion, Fig. 10 shows excellent agreement in spherical polar coordinates between the Mach 4, $\alpha = 20$ deg flowfield structure derived from two PLS "cuts" separated by 33 mm of conical ray length. Both cuts were taken outside the inception zone with the VCO 21 mm ahead of the fin leading edge.

Physical Flowfield Model

As stated earlier, the goal of this study is to produce a comprehensive physical model which describes the flowfield structure and behavior of sharp-fin-generated swept interactions. By combining the information from the present PLS images with results from our previous measurements,[3,4,8] such a model has been constructed in conical ϕ, β coordinates.

Figures 11–16 show the flowfield maps for the six present test cases in order of increasing interaction strength. The ϕ, β coordinates of these maps correspond accurately to the actual locations of the various flowfield features in a conical frame of reference. The overall structure (e.g., λ-shock, separation bubble, and impinging jet) has been obtained from the PLS images, while smaller-scale details were extracted from conical shadowgrams.[8] The uncertainty associated with the location of the features extracted from the PLS images is ±0.5 deg. The indicated locations of the various surface features, where available, were obtained from kerosene-lampblack surface-flow patterns.

In addition to the flowfield maps, scaled plots of the surface pressure[21] and skin-friction distributions,[3] which were available for only five of the test cases, are shown beneath their respective flowfield maps. These plots are crucial to the correlation of surface and flowfield features, and thus to the overall physical model of the flow. The specific features of the model will next be discussed in detail.

Flowfield Features

Because of the past lack of clear flowfield imagery of these interactions, the rear part of the interaction has historically been the least studied and understood. For the first time, the current PLS images give us a clear, overall view of the flowfield structure in this region.

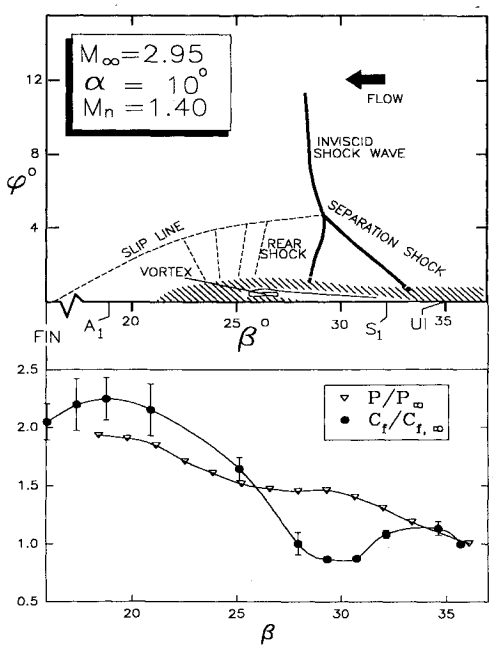

Fig. 11 Flowfield map (Mach 3, $\alpha = 10$ deg).

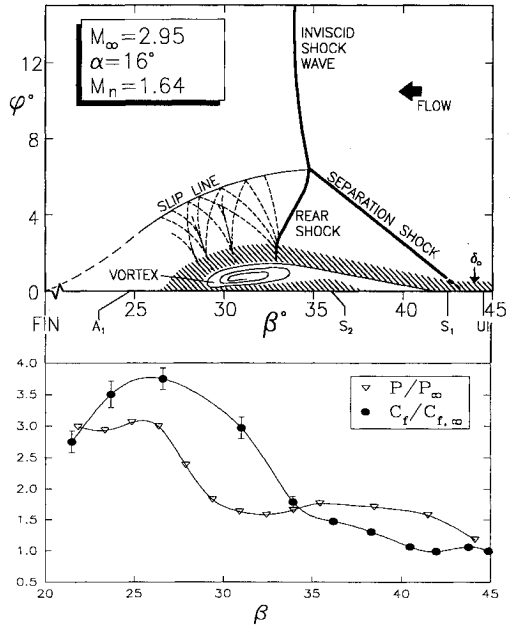

Fig. 12 Flowfield map (Mach 3, α = 16 deg).

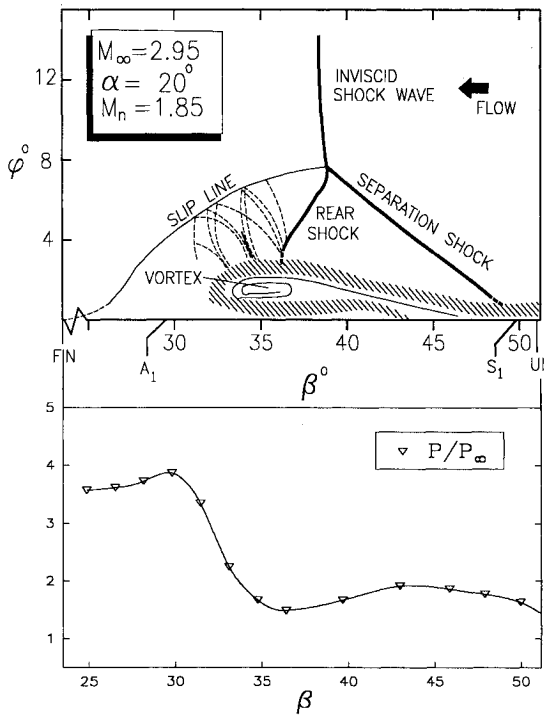

Fig. 13 Flowfield map (Mach 3, α = 20 deg).

Slip Line

The difference in shock strengths above and below the triple point imparts a velocity difference between streamlines passing above and below this point. As a result, a "slip line" or shear layer originates at the triple point. This is understood to be a surface in three-space which projects as a line in the present conical coordinate frame.

For the barely separated interaction of Fig. 11, the density difference across the slip line is too small to be clearly visible in the PLS image (Fig. 4). In this weak interaction, the location of the slip line was obtained from a conical shadowgram of the flow. However, since our conical shadowgrams lacked the accurate reference frame of the PLS imagery, the ϕ, β coordinates of any flow feature derived from them are approximate. Thus the slip line is shown as a broken line for this case in Fig. 11.

For all stronger interactions the slip line is clear in the PLS images. It is observed to converge into the corner formed by

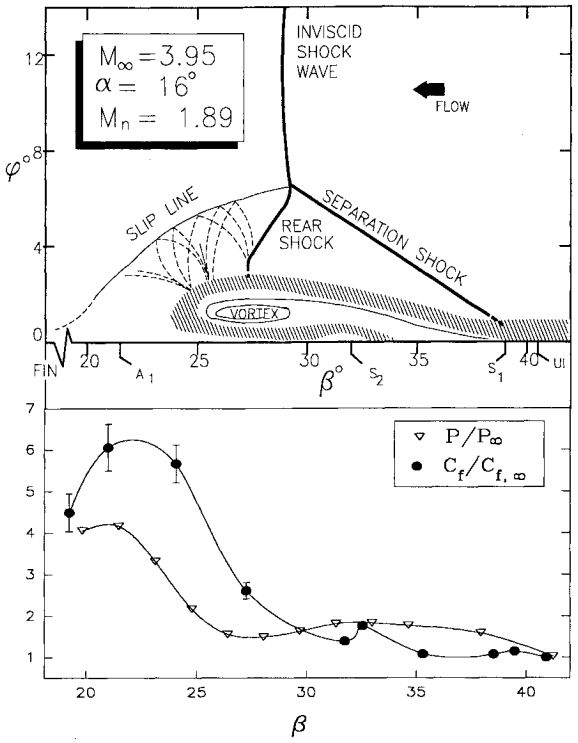

Fig. 14 Flowfield map (Mach 4, α = 16 deg).

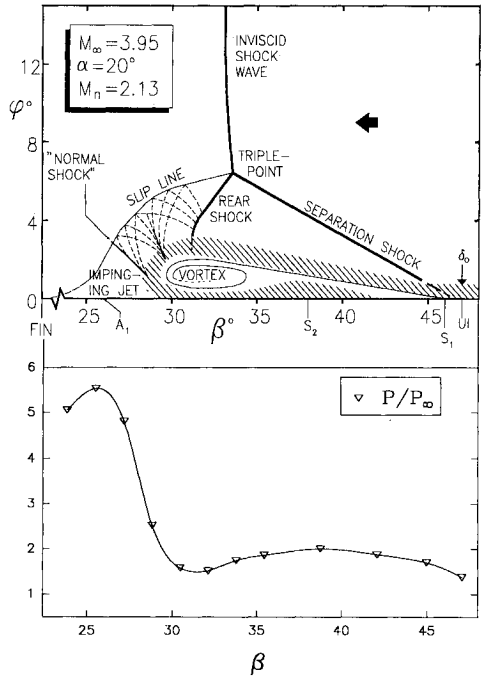

Fig. 15 Flowfield map (Mach 4, α = 20 deg).

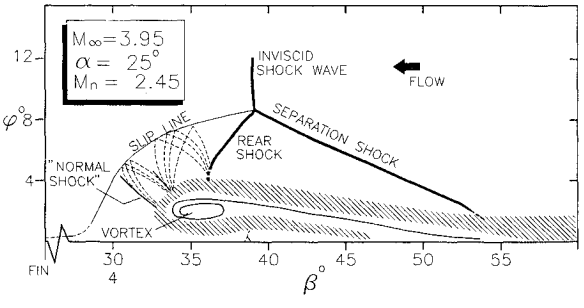

Fig. 16 Flowfield map (Mach 4, α = 25 deg).

the fin and the flat plate. We had suggested this behavior earlier,[8] but had not clearly observed it due to the nature of conical shadowgraphy and the previously mentioned departure from conicity at the fin/plate junction. Also for the latter reason, slip lines are shown as broken lines near the fin/plate junction in Figs. 12–16.

Jet Impingement

The slip line defines the outer boundary and the separation bubble defines the inner boundary of the impinging-jet structure. As observed in the PLS images and drawn in the flowfield maps, this jet curves around the separation bubble and impinges upon the flat plate. This turning is accomplished via a Prandtl-Meyer expansion fan (dashed lines in Figs. 12–16), which reflects from the slip line as a compression fan. For the weakest interaction of the present series (Fig. 11) this turning is very gradual and is accomplished essentially isentropically. The flow in the impinging jet is thus almost featureless with only Mach waves visible in the conical shadowgram.

An increase in the interaction strength has the effect of shortening the distance and increasing the total angle through which the jet has to turn between the rear shock and jet impingement. Thus the local Mach number after the initial jet expansion fan grows larger. The resulting compression fan, after reflection from the slip line, can no longer remain isentropic; it coalesces to form a "shocklet." Figure 17, a conical shadowgram for the Mach 3, $\alpha = 20$ deg case, clearly reveals such a shocklet in the jet structure. In the flowfield maps, these shocklets are drawn as solid lines at the point where the compression waves coalesce.

As the interaction strength further increases, so do the strengths of the reflected compression-fan coalescence. Eventually, the final shocklet in the jet becomes a "normal shock" which terminates supersonic flow in the jet prior to its impingement. Such a "normal shock" is seen in the two strongest interactions of the present test matrix and is marked on the respective flowfield maps. A corresponding flow-regime boundary is indicated in Fig. 3. Please note that this shock wave is approximately normal to the flow in the conical projection, in which framework it is believed to possess all of the attributes usually associated with a normal shock. However, without the benefit of the quasiconical-flow approximation invoked here, this shock would appear to be an oblique shock wave in three-space.

Upon impingement on the flat plate, the jet divides into two streams: the "reversed" flow, which turns forward into the separation bubble, and the "reattached" flow, which turns aft toward the fin. The line along which the jet is thus divided is a line of primary flow attachment; where available from surface flow traces its location is indicated as A_1 on the flowfield maps.

Finally, although the jet grows larger and must turn through a greater total angle as the separation bubble grows, it remains confined by essentially the same angular boundaries (the inviscid shock forward and the fin aft). Consequently, with increasing interaction strength the jet structure appears to become "compacted" in the flowfield maps. Its angle of impingement upon the flat plate increases dramatically over the range of interaction strength illustrated here.

Primary Separation and Vortex Core

The incoming boundary layer, unable to overcome the pressure rise imposed by the interaction, separates to form a free shear layer which subsequently attaches aft of the rear shock. The location of the primary separation line, also obtained from surface-flow patterns, is indicated as S_1 on the flowfield maps. Associated with this is UI, the upstream influence line location, which is the forward-most feature of the interaction footprint.

The separation bubble has been shown both experimentally[22,23] and computationally[11,12,24] to consist of a flattened, spiral vortex. The conical separation streamline, shown in Figs. 11–16, emanates from S_1 and rolls up into the vortex core. Since the PLS and conical shadowgram images show no detail here, the ϕ, β locations of the vortex cores were determined approximately from conical holographic interferograms of these interactions obtained by Hsu and Settles.[23]

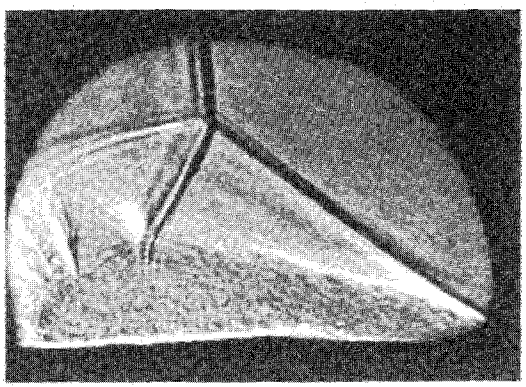

Fig. 17 Conical shadowgram (Mach 3, $\alpha = 20$ deg).

In an "open" separation bubble such as those seen here, separation and attachment streamlines are well known to be distinct. The attachment streamline enters the interaction at some distance above the flat-plate surface, "rides over" the separation bubble, and intersects the flat plate at the primary attachment line A_1. We cannot locate the attachment streamline accurately with our present data, so we have not shown it in any of the flowfield maps.

Secondary Separation

At moderate interaction strengths, a feature commonly referred to as "secondary separation" is first observed inside the primary separation bubble. Our surface-flow patterns show the "secondary separation" line only as a discontinuity in the surface streamlines—not clearly indicative of a true separation zone. The conical shadowgrams reveal an obvious "bulge" in the reversed flow near the surface,[8] but this also is not a clear indication of separation. The location of this feature further coincides with a secondary peak in the skin-friction distributions. Thus, while there is certainly something there, we lack sufficient accumulated evidence to say exactly what it is (see Zheltovodov et al.[25] for further discussion of this issue).

The location of this "secondary separation" feature is marked S_2 in the flowfield maps and is further indicated as a "bulge" in the reversed flow near the surface. Once again, the shape of this feature was found from the conical shadowgrams and is therefore approximate. A corresponding flow-regime boundary for secondary separation has been shown in Fig. 3.

Supersonic Reverse Flow

For very high interaction strengths, acceleration of the flow to supersonic speeds has been observed in the reversed flow inside the separation bubble. This occurrence was first postulated, although not demonstrated, by Zubin and Ostapenko.[6] To our knowledge the phenomenon was first observed in our conical shadowgrams.[8] The region of reversed supersonic flow terminates in a shocklet with an apparent λ-shock structure. The approximate shape and location of this feature is shown in Fig. 16, the flowfield map of our strongest interaction. A corresponding flow-regime boundary has been shown in Fig. 3.

Comparison of Skin Friction and Pressure Distributions with Flowfield Maps

Scaled plots of the surface pressure and skin-friction distributions are combined with the flowfield maps in Figs. 11, 12, and 14. For the Mach 3, $\alpha = 20$ deg and Mach 4, $\alpha = 20$ deg cases only the surface pressure distributions were available. Scaled plots of these distributions combined with their respective flowfield maps are shown in Figs. 13 and 15. The uncertainty associated with the pressure measurements is less than

the size of the symbols, whereas the repeatability of the skin-friction measurements is indicated by vertical error bars.

For stronger interactions, these distributions show a gradual rise from the freestream values of $c_f/c_{f,\infty}$ and p/p_∞ in the forward part of the interaction, followed by a rapid climb to peak values to the rear. This behavior may be explained as follows. Increases in interaction strength have been shown to result in a rapid lateral spread of the separation shock. This produces a long, gradual "precursor" region associated with primary separation. On the other hand, following our earlier discussion of the impinging-jet behavior, the extent of that region becomes more confined as the interaction strength increases. Thus, for strong interactions, the surface properties display a long, gentle rise leading up to a rapid climb to a strong peak near primary flow attachment. As noted before, these features are known to become even more exaggerated at hypersonic freestream Mach numbers.

Finally, as we examine the relative peak locations of $c_f/c_{f,\infty}$ and p/p_∞ in Figs. 11, 12, and 14 we notice that, for some cases, the spline-curve fits through the data points seem to indicate different locations for these peaks. However, the lack of resolution of the data does not allow such a conclusion to be made unequivocally. More detailed measurements are needed before this issue is resolved.

Conclusions

The PLS images, combined with results of previous investigations, have allowed us to construct a comprehensive physical model of this family of interactions. A study of these maps provides a better understanding of the entire flowfield. Some of the more significant conclusions regarding the behavior of these interactions are listed below.

1) The excellent overlap of PLS "cuts" made at two different locations strongly supports the conical symmetry of such flows.

2) The interaction structure develops very rapidly after incipient separation, then more gradually as the interaction becomes strong.

3) Stronger interactions lead to an exaggeration of the jet-impingement phenomenon responsible for flow attachment. This is expected to become even more severe for hypersonic interactions.

4) High surface pressures and skin friction appear in the region of jet impingement. Although this behavior had been previously hypothesized, it is now clearly observed upon comparing the flowfield model with skin friction and surface pressure plots.

5) The impinging jet divides into two streams at the attachment line where the fluid upstream of this line turns forward into the separation bubble. Since the attachment streamline is believed to lie slightly above the boundary-layer edge, this indicates that all of the boundary-layer fluid, and then some, is entrained into the separation bubble.

6) Finally, the flowfield model provide a more comprehensive understanding of the interaction behavior and can be used for a direct comparison with CFD predictions.

Acknowledgments

This work was supported by AFOSR Grant 89-0315, monitored by L. Sakell. The authors gratefully acknowledge the assistance of J. D. Miller, J. W. Naughton, and S. S. Garg with the experiments. We further appreciate the advice of C. Bohren, D. D. Knight, E. Stanewsky, and C. C. Horstman. Finally, this work owes much to the earlier contributions of F. K. Lu.

References

[1]Settles, G. S., and Dolling, D. S., "Swept Shock Wave/Boundary-Layer Interactions," *Tactical Missile Aerodynamics,* edited by M. Hemsch and J. Neilsen, Vol. 104, Progress in Astronautics and Aeronautics, AIAA, New York, 1986, pp. 297–379.

[2]Settles, G. S., and Dolling, D. S., "Swept Shock/Boundary-Layer Interactions—Tutorial and Update," AIAA Paper 90-0375, Jan. 1990.

[3]Kim, K. S., Lee, Y., Alvi, F. S., Settles, G. S., and Horstman, C. C., "Skin-Friction Measurements and Computational Comparison of Swept Shock/Boundary-Layer Interactions," AIAA Paper 90-0378; *AIAA Journal,* Vol. 29, No. 10, 1991, pp. 1643–1650.

[4]Lu, F. K., "Fin-Generated Shock-Wave Boundary-Layer Interactions," Ph.D. Dissertation, Mechanical Engineering Dept., Pennsylvania State Univ., University Park, PA, 1988.

[5]Oskam, B., "Three-Dimensional Flowfields Generated by the Interaction of a Swept Shock Wave with a Turbulent Boundary Layer," Ph.D. Dissertation, Aerospace and Mechanical Sciences Dept., Princeton Univ., Princeton, NJ, Sept. 1976.

[6]Zubin, M. A., and Ostapenko, N. A., "Structure of the Flow in the Separation Region Resulting from Interaction of a Normal Shock Wave with a Boundary Layer in a Corner," *Izvestiya AN SSSR, Mekhanika Zhidkosti i Gaza,* Vol. 3, May–June 1979, pp. 51–85.

[7]Lu, F. K., and Settles, G. S., "Structure of Fin-Shock/Boundary Layer Interactions by Laser Light-Screen Visualization," AIAA Paper 88-3801, July 1988.

[8]Alvi, F. S., and Settles, G. S., "Structure of Swept Shock Wave/Boundary-Layer Interactions Using Conical Shadowgraphy," AIAA Paper 90-1644, June 1990.

[9]Settles, G. S., and Lu, F. K., "Conical Similarity of Shock/Boundary-Layer Interactions Generated by Swept and Unswept Fins," *AIAA Journal,* Vol. 23, No. 7, 1985, pp. 1021–1027.

[10]Inger, G. R., "Spanwise Propagation of Upstream Influence in Conical Swept Shock Boundary-Layer Interactions," *AIAA Journal,* Vol. 25, No. 2, 1987, pp. 287–293.

[11]Knight, D. D., Horstman, C. C., and Settles, G. S., "Three-Dimensional Shock Wave-Turbulent Boundary-Layer Interactions Generated by a Sharp Fin at Mach 4," AIAA Paper 91-0648, Jan. 1991.

[12]Knight, D. D., and Badekas, D., "On the Quasi-Conical Flowfield Structure of the Swept Shock Wave-Turbulent Boundary-Layer Interaction," AIAA Paper 91-1759, June 1991.

[13]McGregor, I., "Development of the Vapour Screen Method of Flow Visualization in a 3 ft × 3 ft Supersonic Tunnel," *Flow Visualization in Wind Tunnels Using Indicators,* compiled by R. L. Maltby, AGARDograph 70, April 1962.

[14]Ariessohn, P. C., Self, S. A., and Eustis, R. H., "Two-Wavelength Laser Transmissometer for Measurements of the Mean Size and Concentration of Coal Ash Droplets in Combustion Flows," *Applied Optics,* Vol. 19, No. 22, 1980, pp. 3775–3781.

[15]Durbin, E. J., "Optical Methods Involving Light Scattering for Measuring Size and Concentration of Condensation Particles in Supercooled Hypersonic Flow," NACA TN 2441, Aug. 1951.

[16]Clemens, N. T., and Mungal, M. G., "A Planar Mie Scattering Technique for Visualizing Supersonic Mixing Flows," *Experiments in Fluids,* Vol. 11, No. 2/3, 1991, pp. 175–185.

[17]Bohren, C. F., and Huffman, D. R., *Absorption and Scattering of Light by Small Particles,* Wiley, New York, 1983, Chap. 13.

[18]Bohren, C. F., private communication, Aug. 1990.

[19]Bohren, C. F., "On the Size, Shape, and Orientation of Noctilucent Cloud Particles," *Tellus,* Vol. 35B, No. 1, 1983, pp. 65–72.

[20]Settles, G. S., Alvi, F. S., and Hsu, J. C., "On the Shock Bifurcation/Jet-Impingement Structure of Swept Interactions and Related Flowfields," *Proceedings of the IUTAM Symposium on Separated Flows and Jets,* Novosibirsk, Russia, 1990, edited by V. V. Kozolov and A. V. Dovgal, Springer-Verlag, Berlin-Heidelberg, 1991, pp. 255–262.

[21]Garg, S. S., and Lee, Y., private communication (unpublished results of surface pressure measurements in swept shock/boundary-layer interactions) 1990.

[22]Hsu, J. C., and Settles, G. S., "Measurements of Swept Shock Wave/Turbulent Boundary-Layer Interactions by Holographic Interferometry," AIAA Paper 89-1849, June 1989.

[23]Hsu, J. C., and Settles, G. S., " Holographic Flowfields Density Measurements in Swept Shock Wave/Turbulent Boundary-Layer Interactions," AIAA Paper 92-0746, Jan. 1992.

[24]Horstman, C. C., "Computation of Sharp Fin and Swept Compression Corner Shock/Turbulent Boundary-Layer Interactions," AIAA Paper 86-1032, May 1986.

[25]Zheltovodov, A. A., Maksimov, A. I., and Shilein, E. K., "Development of Turbulent Separated Flows in the Vicinity of Swept Shock Waves," *The Interactions of Complex 3-D Flows,* edited by A. M. Kharitonov, USSR Academy of Sciences, Inst. Theoretical and Applied Machanics, Novosobirsk, Russia, 1987, pp. 67–91.